The Cryosphere Discuss., 5, 183–227, 2011
www.the-cryosphere-discuss.net/5/183/2011/
doi:10.5194/tcd-5-183-2011

The Cryosphere Discussions

Getting around Antarctica: new high-resolution mappings of the grounded and freely-floating boundaries of the Antarctic ice sheet created for the International Polar Year

R. Bindschadler[1], H. Choi[2], A. Wichlacz[2], R. Bingham[3], J. Bohlander[4], K. Brunt[5], H. Corr[6], R. Drews[7], H. Fricker[8], M. Hall[9], R. Hindmarsh[6], J. Kohler[10], L. Padman[11], W. Rack[7], G. Rotschky[10], S. Urbini[12], P. Vornberger[2], and N. Young[13]

[1]Code 614.0, NASA Goddard Space Flight Center, Greenbelt, MD 20771, USA
[2]SAIC, NASA Goddard Space Flight Center, Greenbelt, MD 20771, USA
[3]University of Aberdeen, Aberdeen, AB24 3FX, UK
[4]National Snow and Ice Data Center, University of Colorado, Boulder, CO 80309-0449, USA
[5]Code 614.1, NASA Goddard Space Flight Center, Greenbelt, MD 20771, USA
[6]British Antarctic Survey, High Cross, Madingley Road, Cambridge, CB3 0ET, UK
[7]Gateway Antarctica, University of Canterbury, Private Bag, Christchurch 8140, New Zealand

[8]Scripps Institute of Oceanography, University of California at San Diego, 9500 Giman Drive, La Jolla, CA 92093, USA
[9]Climate Change Institute, University of Maine, Orono, ME 04469, USA
[10]Norwegian Polar Institute, Polar Environmental Centre, 9296 Tromso, Norway
[11]ESR, 3350 SW Cascade Ave., Corvallis, OR 97333-1536, USA
[12]Istituto Nazionale di Geofisica e Vulcanologia, Via di Vigna Murata, 605, 00143 Rome, Italy
[13]Australian Antarctic Division, University of Tasmania, Kingston, Tasmania 7050, Australia

Received: 28 December 2010 – Accepted: 4 January 2011 – Published: 19 January 2011

Correspondence to: R. Bindschadler (robert.a.bindschadler@nasa.gov)

Published by Copernicus Publications on behalf of the European Geosciences Union.

Abstract

The boundary of grounded ice and the location of ice transitioning to a freely floating state are mapped at 15-m resolution around the entire continent of Antarctica. These data products are produced by participants of the International Polar Year project ASAID using customized software combining Landsat-7 imagery and ICESat laser altimetry. The grounded ice boundary is 53 610 km long; 74% of it abuts to floating ice shelves or outlet glaciers, 19% is adjacent to open or sea-ice covered ocean, and 7% of the boundary are land terminations with bare rock. Elevations along each line are selected from 6 candidate digital elevation models: two created from the input ICESat laser altimetry and Landsat data, two from stereo satellite imagery, and two from compilations of primarily radar altimetry. Elevation selection and an assignment of confidence in the elevation value are based on agreement with ICESat elevation values and shape of the surface inferred from the Landsat imagery. Elevations along the freely-floating boundary (called the hydrostatic line) are converted to ice thicknesses by applying a firn-correction factor and a flotation criterion. The relationship between the seaward offset of the hydrostatic line from the grounding line only weakly matches a prediction based on beam theory. Airborne data are used to validate the technique of grounding line mapping, elevation selection and ice thickness derivation. The mapped products along with the customized software to generate them and a variety of intermediate products are available from the National Snow and Ice Data Center.

1 Introduction

The continental size of Antarctica makes any comprehensive mapping an inherently challenging project. Until satellite remote sensing began to provide large volumes of data, few complete mappings were feasible. Even with extensive satellite coverage, there still are many glaciological features of interest that are still difficult to extract. As sensors have improved and coverage has accumulated, mapping large areas has become more tractable.

TCD
5, 183–227, 2011

One of the most basic features of the Antarctic ice sheet is its boundary. Ice flow and episodic calving cause this boundary to vary with time, a consequence that itself has glaciological value. Much of this boundary is comprised of floating ice shelves, fed by the interior ice sheet and further defined by another boundary – the locus of points where ice in contact with the bed first floats free of that bed – usually called the "grounding line". This transition is conceptually simple, however, the region where it occurs is the site of a dramatic change in the stresses exerted on the ice, challenging modelers of ice flow (see Schoof, 2007 for a recent treatment of the transitional ice dynamics) and where oscillatory tidal forcing on the floating ice shelf moves the precise grounding line daily, leading to a spatially distributed set of grounding line indicators, each associated with some dynamic facet of this grounded-ice to floating-ice transition (see Vaughan, 1995 for a description of the flexure theory supported by field measurements).

These complexities are worth tackling because the grounding line represents a major interface across which the ocean and/or the floating ice shelf can have a large impact on the behavior of the grounded ice sheet and dynamic changes of the grounded ice sheet are amplified as they propagate toward this boundary. The relatively low subglacial bed slopes of grounding line areas (slopes of 10^{-3} to 10^{-5} are typical) amplify relatively small local changes in ice thickness to relatively large horizontal shifts in the grounding line position. Thus, careful monitoring of the grounding line has merit as a sensitive indicator of change. However, to reliably identify positional changes that can be interpreted as having dynamic causes, it is important to be clear in the methodology used and consistent in its application, so that alternate methods do not lead to false conclusions of change.

This paper presents new mappings of the grounded and freely floating boundaries of the Antarctic ice sheet with detailed descriptions of how those products were produced. Surface elevations of the ice along these boundaries are also extracted from various digital elevation data sets along with a calculation of equivalent ice thickness. These are intermediate products of a larger project aimed at quantifying the total ice discharge

TCD
5, 183–227, 2011

of the ice sheet. The data are validated in selected areas where airborne ground truth data are available.

2 The ASAID project

The International Polar Year (IPY) provided motivation for undertaking this project. Among its many objectives, the IPY called for production of benchmark data sets, international collaboration, projects to inspire the next generation of scientists and engineers, and data to be made available universally (ICSU, 2004). In response to this appeal, we conceived a project to quantify the total snow accumulation and total ice discharge from the Antarctic ice sheet called Antarctic Surface Accumulation and Ice Discharge (ASAID). Plans for a collaborative approach to combining surface accumulation data sets from existing and IPY-period ground radar traverses floundered at the proposal stage and were never submitted. The project name remained even though the effort came to focus on only the ice discharge task. This effort initially sought participants in various nations to fly portions of the grounding line with airborne ice penetrating radars to enable quantification of ice discharge; however few airborne assets were available due to other emerging IPY projects. Limited airborne data sets were collected, but the main thrust became one resting on a unique methodology combining data collected by various satellite instruments.

Quantification of the discharge flux will ultimately be achieved by combining a data set of ice flow with a data set of the grounding line boundary that includes ice thickness along that boundary. The production of these two data sets has followed parallel paths. Surface velocity data are being produced from satellite synthetic aperture radar data using both interferometric and speckle tracking techniques (Joughin, personal communication). That effort will add considerable information to previous quantifications of Antarctic discharge flux (Rignot and Thomas, 2002; Rignot et al., 2008), but will not be reported on in this paper. These earlier published assessments focused on fast-flowing glaciers which drain most of the ice-sheet area, but ignored the slower moving

TCD
5, 183–227, 2011

perimeter. Catchment basins along this slower moving perimeter are smaller and confined to the marginal areas, but accumulation rates are high (Arthern et al., 2006; van de Berg et al., 2006). As an example, the fastest 30 outlet glaciers considered by Rignot and Thomas (2002) accounted for less than 50% of the expected total discharge (estimated as a proportion of the calculated accumulation flux) (Fig. 1).

In this paper, we focus on the extracted data of grounding line position and surface elevation along and in the vicinity of the grounding line. In addition, a hydrostatic line, defined as the locus of points where recently ungrounded ice first begins to float freely, is also drawn including the elevation and calculated ice thicknesses along this line. The need for the hydrostatic line comes from the fact that surface elevation can only be converted to ice thickness if the ice is in hydrostatic equilibrium.

3 The grounding line region

As mentioned above, the grounding line occurs in a region where the ice sheet experiences a number of changes. Oscillating ocean tides interacting with the floating fringe of the ice sheet produce regions detectable by various satellite sensors. This has been discussed most completely in Fricker et al. (2009) and is illustrated in Fig. 2. A floating ice shelf extending far offshore can be considered as freely floating and will rise and fall an amount equal to the tidal variations of the ocean in which it floats. However, closer to shore, the stiffness of the ice and the fact that ice well inland is securely resting on the subglacial bed (be it above or below sea level) will limit the amount of vertical deflection experienced within the marginal region. In Fig. 2, location F refers to the most seaward point not vertically displaced by tidal flexure; G is the location where the ice loses contact with the bed (at low tide); l_b and l_m represent inflections of the surface slope where the slope changes most rapidly (the "slope break") and where the slope is zero (the "hingle line valley"), respectively; and H is the most landward location that experiences full tidal flexure.

TCD
5, 183–227, 2011

As discussed below, the ASAID grounding line is determined primarily by interpreting optical imagey and secondarily from derived surface elevations, so it is most consistent with point l_b, the slope break. Interferometric analysis of synthetic aperture radar data usually detect the band of flexure between locations F and H, and repeat laser altimetry can often detect F and H from repeat-track analysis and l_b and l_m from single profiles (Yamanokuchi et al., 2005; Fricker et al., 2006). Figure 3 illustrates results from these different approaches for a portion of Antarctic margin near the Ekstroem Ice Shelf and Neumayer Station. There is broad agreement between the region of flexure zone, defined by the band of dense InSAR fringes, the l_b and H points, defined by the GLAS analysis, and the delineation of the grounded ice boundary, interpreted from the Landsat imagery (discussed in more detail later). However there are some differences, such as in the upper left of the scene where the flexure zone narrows while the hydrostatic line, guided only by the few GLAS points remains farther offshore. In the inlet on the right side of Fig. 3, the ASAID grounding line passes farther landward than the band of dense InSAR fringes, but in agreement with the l_b point determined from GLAS. There will always be some differences between grounding lines produced by these different methods, at times due to incorrect interpretation or data quality and availability, but also because different features are being detected.

Explicit in the definition of grounding line is the transition from grounded ice to floating ice, so it strictly only applies to the situation where there is floating ice adjacent to the grounded ice and it is usually assumed that this floating ice is dynamically attached, as in the case of an ice shelf fed by grounded ice flow. However, there are portions of the boundary of the Antarctic ice sheet where the grounded ice sheet either calves off cliffs into the ocean or gradually thins on land as in land-terminating glaciers. We include these types of boundaries in our product which can more correctly be referred to as the grounded ice boundary of the ice sheet, but recognize that this more general boundary is often called the “grounding line”. Henceforth in this paper, we do not draw a distinction between these two terms.

TCD
5, 183–227, 2011

Previous mappings of the "grounding line" have been produced and made available through data centers. Two of these familiar to many Antarctic users are, first, the grounding line contained in the Antarctic Digital Database (http://www.add.scar.org:8080/add/index.jsp) where the latest revisions were based on prints of Landsat imagery at 1:250 000 scale and, second, a grounding line mapped from the MODIS Mosaic of Antarctica (MOA) at 125-meter resolution (Bohlander and Scambos, 2007). A third partial mapping is being released as coastal change maps (Ferrigno et al., 1996 and http://pubs.usgs.gov/imap/2600/). Each of these mapped boundaries corresponds to either the most rapid change in surface slope (e.g., I_b in Fig. 2) – a locally concentrated "slope break" often is evident where the sloped grounded ice transitions to a relatively flat surface of floating ice – or an end of grounded ice (in the case of terminating ice cliffs or grounded glacier tongues). Because each uses a similar visual interpretative method to ASAID, they are comparable to each other and to the ASAID grounded ice boundary. Figure 4 illustrates difference, large and small, between these various grounding line products.

4 Data

The primary data sets used to define and provide surface elevations of the grounded ice boundary and hydrostatic line were images from the Enhanced Thematic Mapper Plus (ETM+) instrument onboard the Landsat-7 satellite and surface elevation profiles measured by the Geoscience Laser Altimeter System (GLAS) onboard the Ice, Cloud, and Land Elevation Satellite (ICESat) . The Landsat data were Enhanced Thematic Mapper Plus (ETM+) images collected onboard Landsat-7 and used in the construction of the Landsat Image Mosaic of Antarctica, another IPY project (Bindschadler et al., 2009). This image set consists of mostly high quality, cloud-free images. They also cluster within a relatively narrow time window (1999–2003) All images were accessed from the USGS EROS Data Center, usually by ftp-download after a visual review of possible candidate images that covered the appropriate region of the ice sheet perimeter. 196

TCD
5, 183–227, 2011

images of this collection covered the entire grounded ice boundary to 82.5° S. Farther south, two ASTER images provided coverage that completed the Ronne Ice Shelf portion of the grounded ice boundary, and imagery from MOA was used to complete the sourthernmost section of the Ross Ice Shelf. For all but the MOA imagery, the panchromatic band image was visually interpreted at full 15-m resolution (panchromatic band) to identify either the grounding line or the physical edge of the ice sheet, in the case of ice cliffs or glacier tongue termini (cf., Fig. 4).

GLAS/ICESat data of precise surface elevation information along satellite groundtracks were used in three different ways. First, single profiles were used to define the locations of the point of most rapid slope change l_b. These points were used to help confirm the identification of the grounding line tht was based primarily on the imagery. Second, profiles collected at different phases of the tide but along repeat tracks were analyzed by means of a differencing technique that revealed the tidal flexure of the ice shelf and allowed the identification of H locations used to map the hydrostatic line, as described in Fricker et al. (2006) (cf., Fig. 2). These two uses employed the set of F, l_b and H points available from the National Snow and Ice Data Center (Brunt et al., 2010b). The third use of the GLAS elevation profile data were in combination with the ETM+ images to produce surface elevation fields. The combination of surface elevation profiles and optical imagery for the production of surface elevation fields is called photoclinometry (Wildey, 1975; Bindschadler and Vornberger, 1994). It uses image shading to quantify surface slopes that are then integrated between profile points of known elevation. It has been extensively developed for ice sheets where the existence of a homogenous surface of nearly constant albedo satisfies an important assumption for successful application of the technique. Details of the application are discussed below and Fig. 4 shows an example derived elevation field.

TCD
5, 183–227, 2011

5 Methods

To satisfy the IPY objectives of international collaboration and inspiring young researchers, the ASAID project invited partners across the world to participate. Customized software was created, along with appropriate documentation describing standardized procedures so that the eventual aggregate product was as uniform as possible. The Antarctic perimeter was divided into a number of segments with different ASAID participants accepting responsibility for mapping portions of the grounding line and producing photoclinometric elevation fields for that segment (the hydrostatic line and elevation selection were completed at the end of the project exclusively at NASA Goddard Space Flight Center). The software was designed so that the participant's results were written to files with standardized names, facilitating both review of the data at NASA Goddard, but also easing the combination of multiple participant results into a single aggregate. Ultimately, all data products were reviewed by the Principal Investigator (Bindschadler) and final responsibility for their content and quality rests there.

5.1 Grounding line

Our procedure starts with selecting a particular ETM+ image covering the desired section of the Antarctic perimeter and downloading it from USGS EROS Data Center website. The ASAID software uses the image metadata supplied with the image to determine the sun azimuth for the image and rotates the image to a sun-at-the-top orientation (required for the later photoclinometry procedures). The software then displays the rotated image on a computer monitor and superimposes the location of ICESat reference groundtracks on the image. Actual groundtracks usually lie within 100 m of the reference groundtracks. Next, to reduce computer memory requirements and file sizes, the user defines sub-images to work on that encompass sections of the expected grounding line and include ICESat tracks near the top and bottom edges of the sub-image so a photoclinometric DEM spanning most of the sub-image can be produced. Once the sub-images are defined, each is written to a separate file directory

TCD
5, 183–227, 2011

and the GLAS data for that region are parsed from the complete set of GLAS data (provided to each ASAID user) and also written to the same directory. The GLAS data used were the GLAS06 product from observation periods 2A (4 October 2003 to 19 November 2003) through 3K (4 October 2008 to 19 October 2008).

At this point, the user visually reviews the individual GLAS profiles for each reference track (using custom software provided) and selects the profiles most suitable for photoclinometry. Only one profile for each reference track is permissible. Averages were not used because individual profiles were not spatially coincident, but separated by tens and sometimes hundreds of meters. The "best" profile was usually the most continuous profile, but the coastal region of Antarctica is often cloudy, producing large and/or multiple gaps in the profiles. Our application of photoclinometry required a GLAS elevation both up-sun and down-sun (vertical screen lines on the reoriented image) as starting and ending points for the interpolated elevations. This requirement sometimes influences the decision of "best" profile so there will be derived elevations at the grounding line.

Photoclinometry is then applied within the sub-image to produce elevation values at all image points between GLAS profiles based on the image pixel brightnesses. Image pixel brightness is related to surface slope by

$$\mathrm{DN} = A\cos\theta + B \quad (1)$$

where DN is the pixel brightness (in units of digital number); θ is the angle between the solar illumination and the surface normal; the coefficient A is the product of the solar irradiance, the surface reflectivity and the factor converting radiance to sensor DN units; and B is a bias due the sensor zero-radiance offset and atmospheric scattering (Bindschadler and Vornberger, 1994). In most ice sheet situations, B is negligible and we also chose to make this assumption. Equation (1) is applied independently for each image segment lying between an up-sun GLAS profile and a down-sun GLAS profile. Segments are kept as short as possible to minimize interpolation errors. To ensure that the GLAS profiles were continuous at the pixel scale, each profile is linearly interpolated across the standard GLAS point spacing of about 170 m as well across data gaps

TCD
5, 183–227, 2011

as large as 450 m. Larger gaps remain unfilled and can create larger gaps in the elevation field. For each image segment, Eq. (1) is applied after solving for that segments' unique value of the scaling coefficient, A, using values of the average slope and image brightness along that segment. This method ensures that the GLAS elevations along profiles remain unchanged although it does produce slight discontinuities between adjacent image segments when the scaling parameters for adjacent image segments vary significantly (these artifacts are sometimes referred to as "curtains") because at increasing distance from an GLAS profile they can produce a sudden cross-profile discontinuity in the elevation field. Alternative implementations of Eq. (1) were considered, but the GLAS data were deemed to be the best-known elevation information, relative to the possibility of constant albedo and the precision of the Landsat brightness values and the assumption of constant albedo, so these values remain fixed. Figure 4 shows the pattern of selected GLAS profiles for a representative portion of Antarctica and the elevation field derived from photoclinometry. The angled boundaries of the elevation field result from the requirement that there be an up-sun and down-sun GLAS elevation point.

While photoclinometry was very successful over much of the ice sheet perimeter, conditions of albedo variation not related to surface slope were encountered in some regions that made portions of the photoclinometric results unusable. These conditions included open (dark) ocean, exposed rock and open crevasses. An alternate elevation field was created from the GLAS elevations by applying a Delaunay triangulation scheme. In this instance, only the GLAS data were used; the image data were ignored entirely. The quality of the result varied by location, dependent primarily n the density of GLAS profiles, but also on the topographic variation of the region. Other, more sophisticated interpolation methods were examined, but they had the propensity for very large errors over sparsely sampled, undulated topography. Ultimately, our more conservative approach was deemed preferable because it provided an elevation value close to the GLAS values and was reliable in providing a value when no other elevation methods worked.

TCD
5, 183–227, 2011

At this stage, with the image providing a nadir view of the sub-image region and the derived elevation field providing a view of the three-dimensional shape of the area, the grounding line was drawn. Both data sets were linked in separate displayed windows on the computer monitor so that cursor movements could be followed in both windows. To assist the user, the displayed range of either gray-scale (of the image) or color scale (of the elevation field) could be adjusted and the user could zoom the displays to view detail at the 15-m pixel level. Guiding the cursor, the user either drew a continuous line, or clicked discrete points that the computer connected with linear segments, displaying the new grounding line on the image. The MOA grounding line was also displayed and provided useful guidance in areas where the ETM+ radiometric resolution (even with adjustable contrast applied by the user) failed to resolve important subtleties of the surface. Just as often, the increased spatial resolution of ETM+ enabled corrections to the MODIS grounding line (cf., Fig. 4).

The primary visual guide to tracing the grounding line was a change in image brightness that corresponded to the localized slope break between a relatively steep slope on the grounded ice and a relatively shallow slope seaward. The smoother surface of the either the floating ice shelf or the fast sea ice relative to the more undulated surface of the grounded ice emphasized this boundary. Marine features, such as offshore icebergs, sea ice lead and floe structures, or open ocean assisted in identifying non-grounded regions. However, even with these numerous clues, defining the boundary at the full 15-m resolution was often challenging, as the spatial scale of the transition was often many pixels wide. In some regions, the GLAS profiles were useful in precisely locating the point of maximum slope change and the software allowed single profiles to be displayed with a linked cursor function that tied position along the profile to image at the single pixel level.

Bare rock was also very easily identified, but uncertainty regarding the possible presence of seasonal snow often required judgments as to the inclusion or exclusion of individual patches of bare rock within the ice sheet boundary. These situations often had a fractal nature to them and some smoothing was applied by both the operator and

TCD
5, 183–227, 2011

by post-drawing software (described later) to be practical. Some false extension of the ice sheet is possible due to seasonal snow and regions prone to this effect should be carefully considered in future monitoring of the ice sheet boundary.

The most challenging sections of the grounding line to identify were where fast-moving glaciers fed ice shelves. In these cases, the glacier was readily identified by surface undulations and the ice shelf by the absence of similar undulations, but the specific boundary between the two was frequently problematic. In general, the grounding line was drawn seaward of the most downstream undulations and other features that appeared to be formed by ice flow over regions of basal resistance, and upstream of ice shelf features such as ice rumples or isolated ice rises. The shallow surface and bed slopes in this type of region are well documented as is the ephemeral, partial grounding that occurs leading to the concept of a grounding zone rather than a line (e.g., Schmeltz et al., 2001). Interferometric synthetic aperture radar (InSAR) analysis has proven particularly helpful in identifying fully and partially floating areas in such regions (Yamanokuchi et al., 2005; Fricker et al., 2009 and cf., Fig. 3), but these InSAR-derived products are not generally available around the continent and are not included in our data set. Analysis of the tidal variations of repeated GLAS elevation profiles (discussed more in a later section) have helped in the few instances where the profiles cross a glacier/ice shelf transition. Thus, for the reasons stated above, the precise location of the grounding lines of outlet glaciers should be viewed with caution, rather the value of our grounding line in these locations is marking the boundary between surface undulations of grounded ice and the smoother regions of floating ice.

The work described above was completed for each sub-image, each in its own file directory. Combining these individual segments into a single continuous grounding line around the entire central ice sheet involved many additional steps. Each sub-image grounding line was visually reviewed and, if necessary, revised, amended or corrected. There were 319 individual segments that were combined. Gaps and overlaps between segments were corrected with additional editing. The two largest gaps occurred south of 82.5° S, beyond Landsat coverage. On the Ronne Ice Shelf, three ASTER images

TCD
5, 183–227, 2011

were used as in an equivalent manner and on the Ross Ice Shelf, the MOA image was used, also as a proxy for Landsat imagery. In these areas, ICESat coverage is plentiful, and the photoclinometric DEMs are high quality, providing an excellent information base from which the grounding line was drawn. Finally, to remove the unavoidable "jitters" and "stair-steps", inherent in either a hand-drawn or piecewise-linear line, the drawn lines were smoothed before joining segments. The smoothing approach used a forward-looking algorithm wherein the direction of the redrawn grounding line was guided by the direction of the next few drawn points rather than only the next point. The details of this approach are provided in separate documentation that will accompany the archived data files (discussed later).

Figure 5 shows the final grounded ice boundary produced by these procedures. It is 53 610 km long and contains 3 574 365 points at a 15-m resolution. The convoluted nature is less apparent at this scale, but for comparison's sake, the length of the 72° latitude line is 12 350 km. The colors in Fig. 5 indicate the nature of the ice transition at each point along the grounded ice boundary. This boundary was set to one of five categories: ice shelf; outlet glacier; fast (sea) ice; open ocean; and rock. The relative sizes of these transition categories is given in Table 1 and in the Fig. 5 caption. Each of these categories had nuances that made them sometimes difficult to discern. The common characteristics applied to define the outlet glacier class were: a spatially confined flow region, the presence of flow stripes oriented along the expected flow direction, and/or the presence of features on the ice shelf suggestive of a concentrated discharge from the grounded ice sheet. The extent of the outlet glacier was usually taken as the cross-flow "gate" and did not include any margin-parallel segment (that being assigned as an "ice shelf" transition). Differences between the categories of fast ice (which includes possible seasonal sea ice) and open ocean are ephemeral, depending on the specific date of the image used. On-land terminations where the ice sheet thins to zero adjacent to bare rock were sometimes confused by seasonal snow cover.

TCD
5, 183–227, 2011

Nearly 3/4 of the ice passing the grounded ice boundary line transitions to an ice shelf (the combination of the ice shelf and outlet glacier categories). This is the fraction of the boundary that corresponds to the properly defined grounding line, where the subglacial bed is submarine at this transition. The fast ice and open ocean categories combine to a sub-total of 19% of the grounded ice boundary, indicating that portion of the ice sheet that flows directly into the ocean and is not connected to an ice shelf fed by the grounded ice. Finally, 7% of the grounded ice boundary, the vast majority of which occurs in the Dry Valleys region near the northwest corner of the Ross Ice Shelf and the northeastern Antarctic Peninsula terminates on land above sea level. This relatively high value is associated with the extreme serpentine nature of the grounding line in these valley incised mountains and includes a few, relatively small, outlet glaciers that terminate on land.

5.2 Hydrostatic line

The hydrostatic line was mapped using the same ASAID software, but rather than following a brightness feature in satellite imagery, it was drawn such that it passed through each H point supplied in the $F/I_b/H$ data set derived from repeat-track analysis of GLAS profiles. Between these points, the hydrostatic line was drawn to reflect the general shape of the grounding line. The smoother shape of the hydrostatic line is intentional, expressing the diffusion of beam supporting stresses onto the ice shelf and has been noticed in interferometric data analyses.

The hydrostatic line can only exist where there is floating ice mechanically connected to the grounded ice sheet, so it is discontinuous around the ice sheet. It occurs predominantly where the transition from grounded ice was to either an ice shelf or an outlet glacier, but included a few places where the grounding line wraps around a coastal nunatak and a continuous ice shelf exists on the seaward side of that nunatak. In some areas, there were no, or widely spaced H points, however, in general, the seaward offset of the hydrostatic line from the grounding line varied only slowly along the hydrostatic line, increasing our confidence that a reasonably accurate mapping of this feature

TCD
5, 183–227, 2011

is possible. An analysis of the seaward offset of the hydrostatic line from the grounding line appears later. Overall the hydrostatic line contains approximately 1.67×10^6 points for a total distance of 27 521 km, considerably shorter than the grounding line, reflecting its smoother, discontinuous nature.

5.3 Elevations

The assumptions required for accurate photoclinometry were violated frequently enough and GLAS elevations were sparse enough that the assignment of elevations to both the grounding line and hydrostatic line points required the inclusion of additional elevation products. There are a number to select from, but each has weaknesses in particular regions or is incomplete, so no single elevation data set was sufficient by itself. Thus, our approach became one of considering a number of elevation values in parallel and selecting the "best" based on their adherence to both GLAS data and the shape of the local ice sheet inferred from the imagery and the GLAS data.

The elevation data sets that were considered included the photoclinometric and triangulation DEMs already discussed. In addition, a DEM based on a combination of radar and laser satellite altimetry (Bamber et al., 2008) and another based primarily on elevations in the Antarctic Digital Database (ADD) in coastal areas and ERS-1 radar altimetry in the ice sheet interior which was used by the RADARSAT project data (Liu et al., 2001) were included. The former, called here the "altimetry" DEM, was provided on 1-km postings while the RADARSAT Version 2 DEM was on 400-m postings. Both were resampled to our 15 m grid using a bi-linear interpolation scheme. Finally, two stereo image-based photogrammetric DEMs were included: the G-DEM based on ASTER stereo imagery (http://www.ersdac.or.jp/GDEM/E/index.html) and, in few selected locations, local DEMs based on stereo SPOT imagery provided by the SPIRIT project (another IPY activity) (Korona et al., 2009). All elevation data sets were converted to WGS-84 geoidal heights (i.e., ASAID elevations are referenced to mean sea level).

TCD
5, 183–227, 2011

Additional customized software was developed to accommodate the needs of this elevation-selection task. Here we describe the exercise for the grounding line, but an equivalent application was completed for the hydrostatic line. The work returned to the sub-image level because that was how the photoclinometric and triangulation DEMs were organized. For each sub-image, each DEM grid was interpolated to extract that DEM's elevation values along the trace of the grounding line. These grounding-line-following elevation profiles were displayed superimposed on each other (using distinct colors for each DEM) along with single elevation values corresponding to where GLAS elevation profiles crossed the grounding line. Figure 6 shows an example of the computer screen produced by this software. In additional on-screen windows, the photoclinometric, altimetric, RADARSAT and ASTER DEMs were displayed as shaded relief images, rotated and illuminated to simulate the original Landsat sub-image. These shaded relief images proved to be an excellent means to highlight artifacts in each DEM grid, providing another test of each DEM's fidelity in matching the surface topography (cf., Fig. 6).

With this visual information, the operator was able to select a portion of the grounding line, define the best source of elevation data along that segment, and assign a quality rating of those elevations. GLAS data were regarded as "truth", so elevation values close to the GLAS data were weighted heavily in choosing the preferred elevation source, as well as in rating its quality, but a profile that matched the perceived shape of the surface along the grounding line was also important. The ability to define the segments based on the relative, and shifting, strengths of the various elevation sources was a critical feature of this operation because it accommodated the frequent situation where a strong data set had gaps. This was particularly troublesome for the SPIRIT DEMs that covered only limited areas and for the ASTER G-DEM that was hampered by the application of an inaccurate coastal mask that omitted elevations in regions where it appeared that excellent elevations might have been provided in the unmasked, but unavailable, DEM. An additional category of "sea level" was created to accommodate the many instances of the grounding line occurring with a transition to the open ocean. No

TCD
5, 183–227, 2011

DEM correctly captured the elevation discontinuity at these locations. In these cases, the DEMs were ignored and a geoidal elevation of zero was specified. This occurred in 9% of the grounding line points.

Figure 7 shows the preferred elevation source and the qualitative confidence of that preferred elevation value for each point along the ASAID grounding line and percentage amounts are also given in Table 2. The photogrammetric DEMs (from ASTER and SPOT) were chosen most frequently; nearly a third (33%) of all elevations. The photogrammetric technique was particularly strong along rugged portions of the grounding line. Their percentage of use would have been undoubtedly larger if either more DEMs were produced by the SPIRIT project or the ASTER G-DEM data were not poorly masked. (Note: the unmasked G-DEM data no longer exist but a second version is scheduled for 2011 with the masking issue yet undecided). Photoclinometric elevations were selected 26% of the time, the next most used elevation source. These segments tended to occur primarily along the grounding line of large ice shelves. RADARSAT and the altimetric DEMs were used 17% and 13% of the time, respectively. The triangulation elevations, a worst-case alternative, only needed to be used 2% of the time.

The quality ranking of the grounding line elevations is included in Fig. 7 to indicate the confidence of the selected elevations. Table 3 summarizes the frequency of each confidence class. The "Excellent" ranking occurred 10% of the time and was reserved for those segments where the elevations matched the GLAS elevations very closely: as such, the elevations along these segments are probably accurate to 1–5 m, even some distance from the GLAS points as justified by the validation study presented later. "Above Average" confidence (40% occurrence) was assigned to segments along which there was close agreement with the GLAS elevations and the shape of the profile agreed with a visual interpretation of the imagery (i.e., the simulated image and the actual image were similar). It is difficult to assign a quantitative estimate of errors, but we estimate that the elevations along these segments have a standard error of 5–25 m. Segments ranked with an "Average" confidence in elevations (44% occurrence) displayed more variations between DEMs but with a clear preference for the strongest

TCD
5, 183–227, 2011

DEM. Errors are likely larger for this class and we assign a standard error of 25–50 m. "Below Average" confidence (5% occurrence) usually corresponded to a lack of any strong DEM, with the preference usually assigned to the DEM profile that either most closely matched the GLAS elevations or that best expressed the shape of the elevation surface interpreted from the imagery. Standard errors are likely in excess of 50 m and are perhaps as large as 100 m. In the cases of "Poor" confidence (1% occurrence), there were no good elevations to choose from and it likely that the standard errors exceed 100 m. To ensure consistent application of this qualitative assessment throughout the entire data set, this rating was completed by a single operator. It is based on the ability of the selected elevation to match the GLAS elevations and conform to the shape of the surface inferred from the imagery and shaded relief simulated images. Usually there was an elevation source that could handle the environmental situation – from rugged mountains, where photogrammetry could follow the rapidly varying elevations, to very smooth, nearly featureless terrain, where photoclinometry was strong.

The identical elevation picking procedure was applied to the hydrostatic line. Figure 8 and Table 2 present similar data for the hydrostatic line. The statistics of the preferred elevation source are different from the grounding line. In particular, photogrammetry is only selected 4% of the time. This was partly due to the fact that it was the strongest method in rugged terrain, where there often is no hydrostatic line and the frequently poor masking of the ASTER G-DEM in these regions when there is a hydrostatic line. In its stead, altimetry made a much larger contribution to hydrostatic line elevations, at 368 of the total. This is probably because the smoothing artifact of altimetric data that biases the elevations high at the grounding line where the slope change is most rapid, is less compromising farther out on the ice shelf. Photoclinometry also increased its share, to 37%, while RADARSAT elevations were used about as frequently as for the grounding line. Sea level was chosen less frequently because a hydrostatic line was not included in open ocean regions.

The qualitative confidence ratings of the hydrostatic line are included in Fig. 8 and Table 3. These were evaluated in a manner consistent with the grounding line elevation

TCD
5, 183–227, 2011

confidences and by the same operator. Overall, the confidence is lower, with lower occurrence in both the "Excellent" and "Above Average" confidence ranges and more frequent cases of "Average" confidence.

5.4 Equivalent ice thickness

Surface elevations were sought primarily for the purpose of converting surface elevation to equivalent ice thicknesses; this requires the ice be in hydrostatic equilibrium, thus, this conversion is valid along the hydrostatic line (and seaward). To complete this conversion, however, the air contained in the surface snow must be accounted for. This is commonly referred to as the "firn depth correction". A detailed meteorological model quantifying this effect has been published by van den Broeke et al. (2008) and we were provided a file specifying the correction term over the Antarctic continent. The conversion relationship is

$$H_e = \frac{(z_s - \Delta h)\rho_w}{\rho_w - \rho_i}; \quad \Delta h = h_f\left(1 - \frac{\rho_f}{\rho_i}\right) \tag{2}$$

where H_e, is the equivalent ice thickness; Z_s is the surface elevation above sea level (referenced to the WGS-84 geoid), h_f and ρ_f are the depth and density of the firn, respectively; and ρ_i and ρ_w are the densities of pure ice and seawater: 917 and 1026 kg/m^3, respectively. The term Δh is the firn-depth correction. It was provided on a 0.1 degree grid and bi-linearly interpolated to the location of each point along the grounding line and hydrostatic line. The distribution of this firn correction term around the perimeter of Antarctic was confirmed to be equivalent to Fig. 4 in van den Broeke et al. (2008).

In applying Eq. (2), there were a few instances where the firn depth correction exceeded our surface elevation leading to negative equivalent ice thicknesses. This is clearly incorrect. Such occurrences were distributed widely around the continent and are often associated with where our hydrostatic line extends across short patches of fast ice between longer sections of floating ice shelf. The single largest concentration

TCD
5, 183–227, 2011

of very low elevations occurs between longitudes 40° E and 57° E. To avoid negative thicknesses, a variable coefficient was added to Eq. (2) modifying it to

$$H_e = \frac{(z_s - f\Delta h)\rho_w}{\rho_w - \rho_i}; \quad f = 1 - e^{\frac{z_s}{\Delta h}} \tag{3}$$

The coefficient, f, is only significant when the firn correction depth becomes a significant fraction of the surface elevation. f ranges from unity for large surface elevations to zero when the firn depth correction is much larger than the surface elevation. Physically this coefficient can be interpreted as reducing the effect of included air in firn when the surface elevation is so low that much of that firn would be flooded by seawater and, presumably refrozen, thus increasing the density and reducing the air content.

Figure 9 shows the distribution of calculated hydrostatic line ice thicknesses around the continent along with a histogram of values. In the map representation, very thick ice (sometimes over 2000 m) occurs where deep ice streams and glacier feed the Ross, Ronne/Filchner and Amery ice shelves. The histogram in Fig. 9 approximates a log-normal distribution but with two unusual features. The first is the local minimum/local maximum couplet at 800–900 m thickness for which we offer no explanation other than to suggest it is an artifact. The second is the high frequency of occurrence at very small ice thicknesses; 6% of the equivalent ice thicknesses are less than one meter. This might be a real feature, reflecting the frequent occurrence of thin ice, but it also is caused, to some undetermined degree, by errors in measurement of thin coastal ice and the accuracy of geoid knowledge along the Antarctic coast. We do not attach any special significance to the observation that the most frequent ice thicknesses are in the range 300–400 m.

A hazard in converting surface elevations to ice thicknesses is the amplification of errors by roughly a factor of ten. In our case this error amplification is unavoidable, but it bears repeating that the user of these ice thicknesses should be very aware of the confidence ratings applied to the hydrostatic line elevations discussed earlier.

TCD
5, 183–227, 2011

6 Validation

Various ASAID participants collected or provided either new or existing data to validate the ASAID products. A particularly useful data set was collected for ASAID validation purposes along extensive reaches of the western boundary of the Ronne Ice Shelf by the British Antarctic Survey (BAS) in the 2006–2007 austral summer. Because the ASIAD mapping of the groundling and hydrostatic lines had not been in that region at the time of the field survey, the grounding line used for flight planning was provided by Ian Joughin (personal communication) from interferometric SAR (InSAR) analysis. Both surface elevation and ice thickness were measured by separate instruments on the Twin Otter aircraft. Approximately 1500 flight kilometers of data were collected along the grounding line. Figure 10 shows the locations of these flights relative to the ASAID grounding line and hydrostatic line. Every tenth point was selected from the BAS flight data files to create a sample spacing of about 200 m and the nearest ASAID grounding line and hydrostatic line points identified. This subset consisted of roughly 7000 points.

The two grounding lines agree extremely well over much of their lengths, but as was discussed earlier, by assigning the InSAR grounding line to the landward edge of the grounding zone (cf. point F in Fig. 2) it should occur more interior to the ASAID mapping of point l_b. This effect is seen most clearly on the Evans Ice Stream where the InSAR grounding line is much farther inland and to a lesser extent at Institute Ice Stream (cf., Fig. 10). Across Carlson Inlet, two flights bracketed the InSAR grounding line with the ASAID grounding line agreeing well with the downstream flightline. Elsewhere, along the seaward boundary of Skytrain Ice Rise and near the southern limit of the BAS flights, the InSAR grounding line is only slightly inland of the ASAID grounding line. Even with these differences in the target being mapped, the mean distance between the grounding line flown by BAS and the ASAID grounding line is 2.86 ± 4.70 km. It is worth repeating here that our grounding line was also checked against the independently identified collection of grounding line points using repeat GLAS profiles and agreed to

TCD
5, 183–227, 2011

better than 1 km in most cases; specific GLAS-path crossings of the grounding line can be examined with the archived data (discussed later).

Because photoclinometry produced the preferred elevations in this region and this method produced an elevation field rather than elevations only along the ASAID grounding line, a direct comparison of elevations at identical flightline locations was possible. The elevation differences (BAS minus ASAID) produced a Gaussian distribution with a mean difference of 0.475 m and a standard deviation of 5.53 m. It is possible that a portion of the elevation differences are real, caused either by dynamic changes or the timing of meteorological events between the early 2000 dates of the GLAS data and the Landsat imagery and the 2006–2007 period of BAS data collection. And it is worth noting that the region appears to be undergoing slight thickening of about 0.2 m/yr (Pritchard et al., 2009). The assigned confidence to these elevations along the nearby ASAID grounding line is roughly divided equally between "Excellent" and "Above Average" (cf. Fig. 7). We used these results to estimate the elevation precisions to accompany the 5-tier confidence scheme presented earlier.

A second comparison focuses on ice thickness, but the locations are not identical and it is more difficult to account for the difference between the BAS measurements and those derived along the hydrostatic line where ASAID ice thicknesses are strongest. We compare the measured ice thickness with the ASAID hydrostatic line ice thickness along with the distance between the thickness locations for three sections of the BAS data set: north of Evans Ice Stream, around Fletcher Promontory and across Institute Ice Stream (cf. Fig. 10). Figure 11 shows the point-by-point comparison across the Institute Ice Stream segment along with histograms of the ice thickness differences for each of the three segments. The histograms show considerable variation in the magnitude of the mean difference. Actual values are: north of Evans, 12.5 ± 77.5 m; Fletcher, -524 ± 289 m; Institute, 46.1 ± 93.6 m. The mean separations between the BAS flightlines and the ASAID hydrostatic lines for the three segments are not significantly different: north of Evans, 8.1 km; Fletcher, 6.5 km; and Institute, 7.8 km.

TCD
5, 183–227, 2011

7 Analysis

In drawing the hydrostatic line, it was noticed that the seaward offset of the GLAS-determined H points from the grounding line was relatively consistent locally, but varied gradually from region to region. This characteristic gave us confidence in interpolating the hydrostatic line between GLAS-determined H points, but here we use our data set to more quantitatively examine this relationship. From a purely mechanical point of view, the seaward offset of the hydrostatic line from the grounding line should depend on the stiffness of the ice, its weight and its thickness. A useful analysis of elastic beam deformation, presented in Vaughan (1995), expresses the beam deflection as

$$w(x) = A_0 \left[1 - e^{-\beta x}(\cos\beta x + \sin\beta x)\right] \tag{4}$$

$$\beta^4 = 3\rho_w g \frac{1-\mu^2}{E h^3} \tag{5}$$

where w is the vertical deflection from mean sea level, A_0 is the full tidal range, ρ_w is the density of seawater, g is gravitational acceleration, μ and E are the viscosity and Young's modulus of ice, respectively, and h is the ice thickness. By examining multiple field data sets, Vaughan (1995) cites a best value of $\beta = 2.43 \pm 0.43 \times 10^{-4}\,\mathrm{m}^{-1}$. For our purposes, we require a relationship between ice thickness and the seaward offset of the hydrostatic line and the grounding line, x_H. For the Rutford Ice Stream examined in Vaughan (1995), x_H is approximately equal to 7000 m, thus $\beta x = 1.7 \pm 0.3$. By substituting this value into Eq. (5) to eliminate β, the following equation relates x_H to ice thickness, h,

$$x_H = 1.7 \left[3\rho_w g \frac{(1-\mu^2)}{E}\right]^{-1/4} h^{3/4} \tag{6}$$

TCD
5, 183–227, 2011

Using standard values for ρ_w and g, and again referring to Vaughan (1995) for values of μ and E (0.3 and 0.88 ± 0.35 GPa, respectively) we arrive at the relationship,

$$x_H = (22.2 \pm 6.2) h^{3/4} \quad (7)$$

This relationship is slightly sub-linear. The only spatially variable parameter in the coefficient is the ice viscosity, a term that varies with ice temperature, but its effect is diminished through the exponent that appears outside the square bracket of Eq. (6).

Figure 12 presents the distribution of ice thickness versus seaward offset of the hydrostatic line from the grounding line for the ASAID data sets. The points plotted were selected as being those closest to the 930 GLAS-determined H points. There is considerable scatter, but the first order relationship of increasing offset distance with ice thickness is borne out and the pattern generally matches the relationship suggested by Eq. (7). Both the varying temperature effect and the firn correction effect contribute to the scatter. The mean offset distance is 3.7 ± 2.2 km and the mean ice thickness is 632 ± 337 m. The locations of thickest ice occur on the Ronne Ice Shelf near Rutford Ice Stream and on the Ross Ice Shelf near Whillans and Mercer Ice Streams. The locations of largest offsets are scattered around the continent without significant clusters. These results agree reasonably well with the grounding zone width values (Ross: 3.2 ± 2.6 km and Ronne: 5.2 ± 2.7 km) by Brunt et al. (2010a) although it is important to note that their grounding zone width is the longer distance from pint F to H, rather than our distance from I_b to H. At best, we can say that our data are consistent with Eq. (6), but it is not possible to use this empirical relationship as a means to define the hydrostatic line from only information on grounding line position and surface elevation.

8 Distribution and archiving

Ensuring the availability of our ASAID products in a useful form to the research is an important objective of this IPY project. The files of the grounding line and hydrostatic line have been generated in such a way to facilitate their use by researchers once

TCD
5, 183–227, 2011

delivered to the National Snow and Ice Data Center (NSIDC). The latitude/longitude coordinates of each point are given along with our preferred surface elevation and its confidence. Also included are the firn correction, the full set of other surface elevations for each point and point coordinates linked to the specific sub-image used to generate that segment of each line. Finally, the grounding line file includes the nature of the grounding line transition (outlet glacier, ice shelf, rock, fast ice or open ocean) and for the hydrostatic line file the converted ice thickness (using Eq. 3 and the preferred elevation and interpolated firn correction). Note, although the grounding line file does include a surface elevation and the interpolated firn correction term, it does not include an ice thickness value calculated from these parameters because we do not wish to encourage use of an ice thickness value that may be seriously in error.

In addition to the basic grounding line and hydrostatic line files, we intend to provide to NSIDC the generating files including the sub-images, line segments, GLAS elevation profiles and derived photoclinometric and triangulation DEMs. It is possible that these files may prove of value either to subsequent research into the data used to produce the higher-order products or to future projects that aim to repeat some or all of what this project accomplished.

Finally, the customized software tools generated for ASAID are also being provided along with detailed documentation in the form of a NASA Technical Memorandum, however software support will not be supplied. The code was written exclusively in IDL so that each ASAID participant could run the various modules using a free-ware IDL engine.

9 Summary and lessons learned

Undertaking this project was facilitated by the existence of the IPY and the primary objectives of this project were strongly influenced by the IPY objectives. This created benefits and disadvantages. The comprehensive nature of the product and the ability to divide the work among many participants were significant characteristics of ASAID,

TCD
5, 183–227, 2011

but the need to create customized software that could run on multiple platforms as well as the need to carefully review and, in many cases, revise submissions from multiple participants were burdensome. Eventually, the ownership of this product by a large international team is a significant characteristic that should establish these products as standards in the glaciological community. In addition, the documentation of the methodology should facilitate future efforts at monitoring both the grounded ice boundary and hydrostatic line. Finally, we are learning that the software and products now available are allowing for the creation of educational activities that promise to increase the impact of ASAID on future scientists.

The production of these data sets now makes what once seemed so daunting appear less so. At a 15-m resolution, Antarctica is monstrously big, but it can be circumnavigated at that scale and the definition of its boundary with the precision achieved by ASAID offers the research community a valuable new benchmark against which changes can be conveniently and accurately monitored and quantified.

Acknowledgement. A project of this magnitude and complexity could not have been accomplished without extensive contributions from many people, some of whom do not appear as authors on this paper. Funding support for the central work was provided through NASA grant 509496.02.08.01.81. Other domestic and international participants have been supported by other funding and we thank the British Antarctic Survey for adding flights specifically for ASAID to an already packed field schedule. Michiel van den Broeke was extremely gracious for providing his work on firn correction values.

References

Arthern, R. J., Winebrenner, D. P., and Vaughan, D. G.: Antarctic snow accumulation mapping using polarization of 4.3-cm wavelength microwave emission, J. Geophys. Res., 111, D06107, doi:10.1029/2004JD005667, 2006.

Bamber, J. L., Gomez-Dans, J. L., and Griggs, J. A.: A new 1 km digital elevation model of the Antarctic derived from combined satellite radar and laser data – Part 1: Data and methods, The Cryosphere, 3, 101–111, doi:10.5194/tc-3-101-2009, 2009.

TCD
5, 183–227, 2011

Bindschadler, R. A. and Vornberger, P. L.: Detailed elevation map of ice stream C using satellite imagery and airborne radar, Ann. Glaciol., 20, 327–335, 1994.
Bindschadler, R. A., Vornberger, P. L., Fox, A. J., Fleming, A. H., and Granneman, B.: The Landsat image mosaic of Antarctica, Remote Sens. Environ., 112, 12, 4214–4226, doi:10.1016/j.rse.2008.07.006, 2008.
Bohlander, J. and Scambos, T.: Antarctic coastlines and grounding line derived from MODIS Mosaic of Antarctica (MOA), Digital Media, National Snow and Ice Data Center, Boulder, CO, USA, 2007.
Brunt, K. M., Fricker, H. A., Padman, L., Scambos, T. A., and O'Neel, S.: Mapping the grounding zone of the Ross Ice Shelf, Antarctica, using ICESat laser altimetry, Ann. Glaciol., 51, 55, 71–79, 2010a.
Brunt, K. M., Fricker, H. A., Padman, L., and O'Neel, S.: ICESat-Derived Grounding Zone for Antarctic Ice Shelves, Digital Media, National Snow and Ice Data Center, Boulder, CO, USA, 2010b.
Ferrigno, J. G., Mullins, J. L., Stapleton, J. A., Chavez, P. S., Velasco, M. G., Williams, R. S., Delinski, G. F., and Lear, D.: Satellite Image Map of Antarctica, US Geological Survey, Miscellaneous Investigations Map Series, Map 1-2560, 1996.
Fricker, H. A. and Padman, L.: Ice shelf grounding zone structure from ICESat laser altimetry, Geophys. Res. Lett., Vol. 33, L15502, doi:10.1029/2006GL026907, 2006.
Fricker, H. A., Coleman, R., Padman, L., Scambos, T. A., Bohlander, J., and Brunt, K. M.: Mapping the grounding zone of the Amery Ice Shelf, East Antarctica using InSAR, MODIS and ICESat, Antarct. Sci., 21, 5, 515–532, doi:10.1017/S095410200999023X, 2009.
Haran, T., Bohlander, J., Scambos, T., and Fahnestock, M. (compilers): MODIS mosaic of Antarctica (MOA) image map, Digital Media, National Snow and Ice Data Center, Boulder, CO, USA, 2005.
Jenkins, A. and Holland, D. M.: A model study of ocean circulation beneath Filchner–Ronne Ice Shelf, Antarctica: implications for bottom water formation, Geophys. Res. Lett., 29, 8, doi:10.1029/2001GL014589, 2002.
Joughin, I. and Padman, L.: Melting and freezing beneath Filchner-Ronne Ice Shelf, Antarctica, Geophys. Res. Lett., 30, 1477, 2003.
ICSU: A Framework for the International Polar Year, 2007–2008, produced by the ICSU IPY 2007-2008 Planning Group; ISBN 0-930357-61-2, 2004.
Korona, J., Berthier, E., Bernard, M., Remy, F., and Thouvenot, E.: SPIRIT. SPOT 5 stereo-

TCD
5, 183–227, 2011

scopic survey of Polar Ice: reference images and topographies during the fourth International Polar Year (2007–2009), ISPRS J. Photogramm. Remote Sens., 64, 204–212, 2009.
Liu, H., Jezek, K., Li, B., and Zhao, Z.: Radarsat Antarctic Mapping Project digital elevation model version 2, Digital Media, National Snow and Ice Data Center, Boulder, CO, 2001.
Pritchard, H. D., Arthern, R. J., Vaughan, D. G., and Edwards, L. A.: Extensive dynamic thinning on the margins of the Greenland and Antarctic ice sheets, Nature, 461, 971–975, doi:10.1038/nature08471, 2009.
Rignot, E. and Thomas, R. H.: Mass balance of polar ice sheets, Science, 297(5586), 1502–1506, 2002.
Rignot, E., Bamber, J. L., van den Broeke, M. R., Davis, C., Yonghong, L., van de Berg, W. J., and van Meijgaard, E.: Recent Antarctic ice mass loss from radar interferometry and regional climate modeling, Nature Geosci., 1, 106–110, doi:10.1038/ngeo102, 2008.
Schmeltz, M., Rignot, E., and MacAyeal, D. R.: Ephemeral grounding as a signal of ice-shelf change, J. Glaciol., 47, 156, 71–77, 2001.
Schoof, C.: Ice sheet grounding line dynamics: steady states, stability, and hysteresis, J. Geophys. Res., 112, F03S28, doi:10.1029/2006JF000664, 2007.
van de Berg, W. J., van den Broeke, M. R., Reijmer, C. H., and Meijgaard, E.: Reassessment of the Antarctic surface mass balance using calibrated output of a regional atmospheric climate model, J. Geoph. Res., 111, D11104, 2006.
van den Broeke, M., van de Berg, W. J., and van Meijgaard, E.: Firn depth correction along the Antarctic grounding line, Antarct. Sci., 20, 513–517, doi:10.1017/S095410200800148X, 2008.
Vaughan, D. G.: Tidal flexure at ice sheet margins, J. Geophys. Res., 100(B4), 6213–6224, 1995.
Wildey, R. L.: Generalized photoclinometry for Mariner 9, Icarus, 25, 613–626, 1975.
Yamanokuchi, T., Doi, K., and Shibuya, K.: Validation of grounding line of the East Antarctic Ice Sheet derived by ERS-1/2 interferometric SAR data, Polar Geosci., 18, 1–14, 2005.

TCD
5, 183–227, 2011

Table 1. Distribution of Antarctic ice sheet grounded ice boundary categories.

Transition category	# of points	
Ice shelf	2 175 363	61%
Outlet glacier	478 883	13%
Fast ice	361 044	10%
Open ocean	325 876	9%
Rock	233 182	7%
Total	3 574 348	100%

TCD
5, 183–227, 2011

Table 2. Elevation Source for points along grounded ice boundary and hydrostatic line.

Source	Grounded ice boundary (%)	Hydrostatic line (%)
Photogrammetry	33	4
Photoclinometry	26	37
RADARSAT	17	16
Altimetry	13	38
Sea level	9	0.3
Triangulation	2	5

TCD
5, 183–227, 2011

Table 3. Elevation confidence for points along grounded ice boundary and hydrostatic line.

	Grounded ice boundary (%)	Hydrostatic line (%)
Excellent	18	4
Above average	36	32
Average	40	59
Below average	5	4
Poor	0.5	0.1

TCD
5, 183–227, 2011

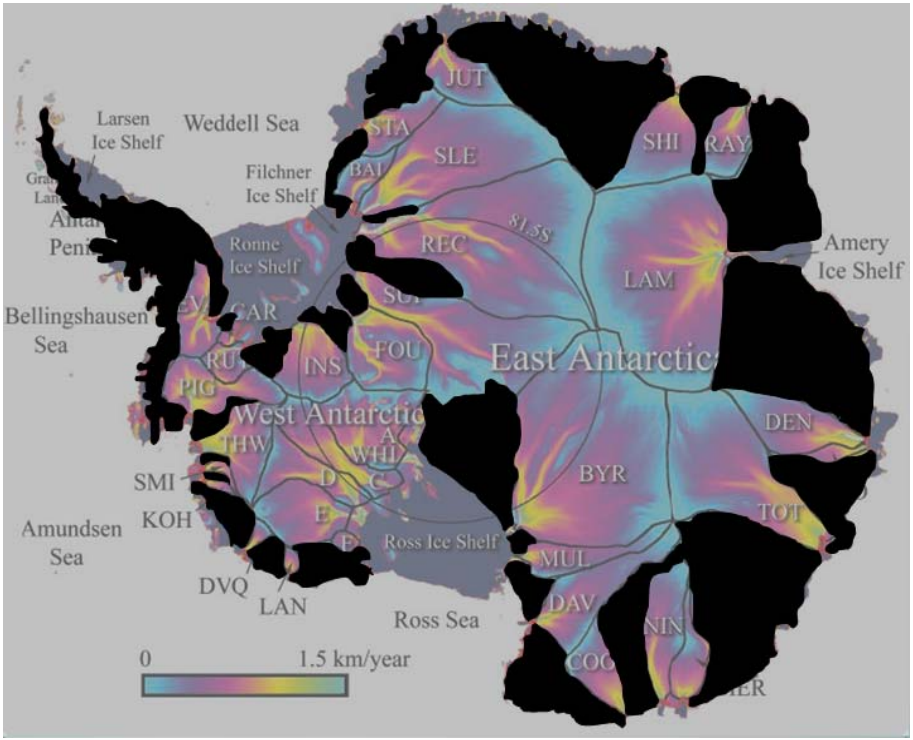

Fig. 1. Map of Antarctica with black areas indicating regions not considered by Rignot and Thomas (2002) in calculating discharge of the 30 largest outlet glaciers (adapted from Rignot and Thomas, 2002).

TCD
5, 183–227, 2011

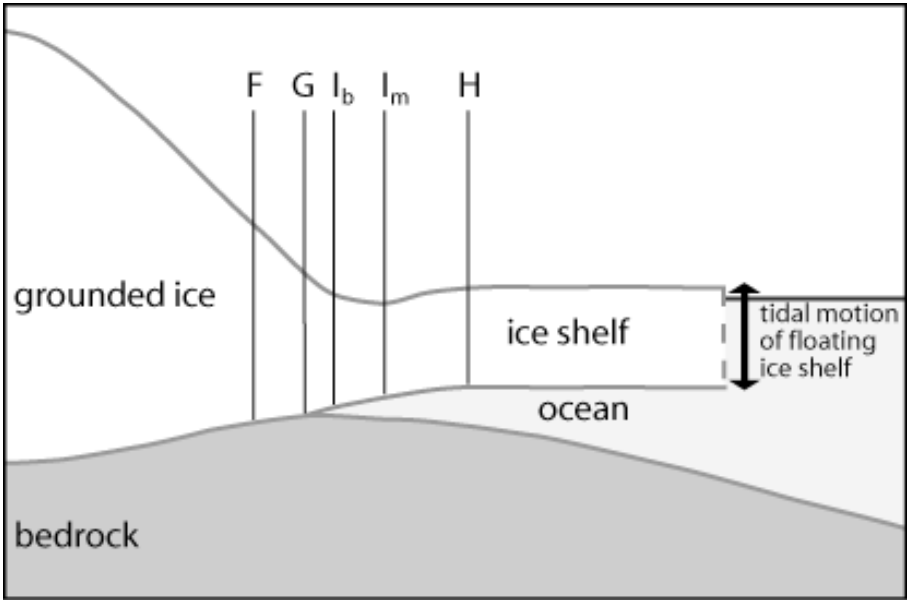

Fig. 2. Schematic of cross-section through the margin of the Antarctic ice sheet. F refers to the most seaward point not vertically displaced by tidal flexure; G is the point where the ice loses contact with the bed (at low tide); I_b and I_m represent inflection points of the surface slope; and H is the most landward point that experiences full tidal flexure. The ASAID grounding line is most consistent with point I_b (from Fricker et al., 2009).

TCD
5, 183–227, 2011

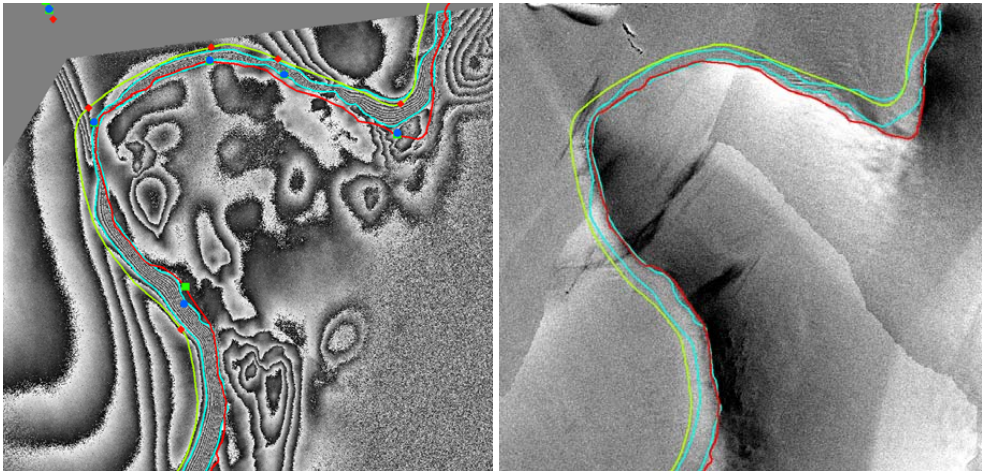

Fig. 3. Section of Antarctic coast (Halvfarryggen Ridge on the Princess Martha Coast with Ekstroem Ice Shelf on left) Image dimensions are 71.6 km×69.7 km comparing mappings of different features of grounding line region with different methods. Left image is interferometric fringe pattern, right image is enhanced subset of Landsat Image Mosaic of Antarctica. Cyan lines represent edges of tidally flexed grounding zone between points F and H (see Fig. 2). Symbols are from repeat-track GLAS elevation profiles (F, green square; I_b, blue circle; H, red diamond). Red and green lines are ASAID grounding line and hydrostatic lines, respectively.

TCD
5, 183–227, 2011

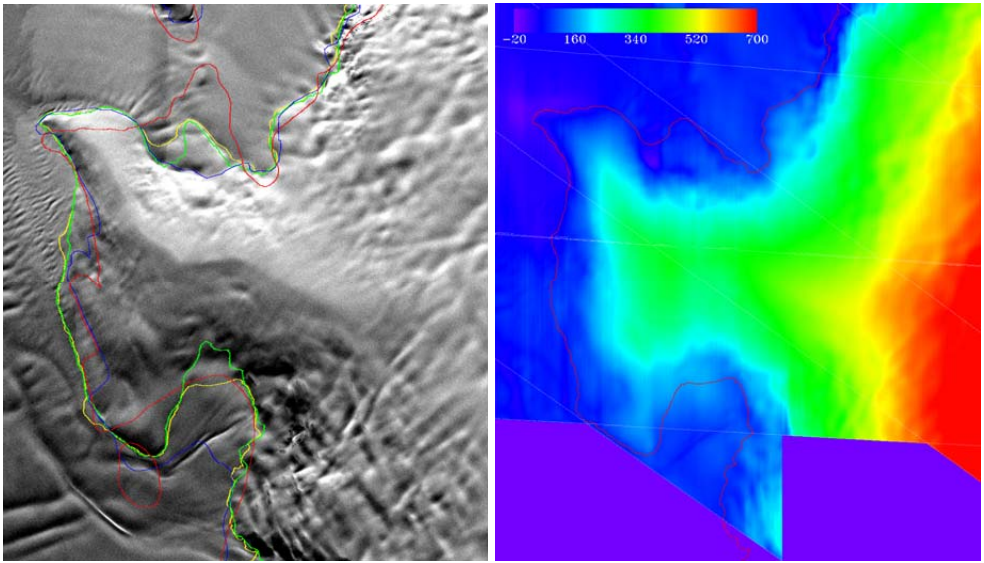

Fig. 4. Section of Antarctic coast (Scott Peninsula along Bakutis Coast) approximately 60 km×69 km. (left) Enhanced Landsat image comparing various image-based mappings of grounding line: red, Antarctic Digital Database; blue, USGS Coastal Change map series; green, MODIS Mosaic of Antarctica; yellow, ASAID. (right) color-coded surface elevations (in meters above mean sea level) derived from ASAID application of photoclinometry using image on left and GLAS elevation profiles. Thin white lines show the location of GLAS profiles interpolated by photoclinometry.

TCD
5, 183–227, 2011

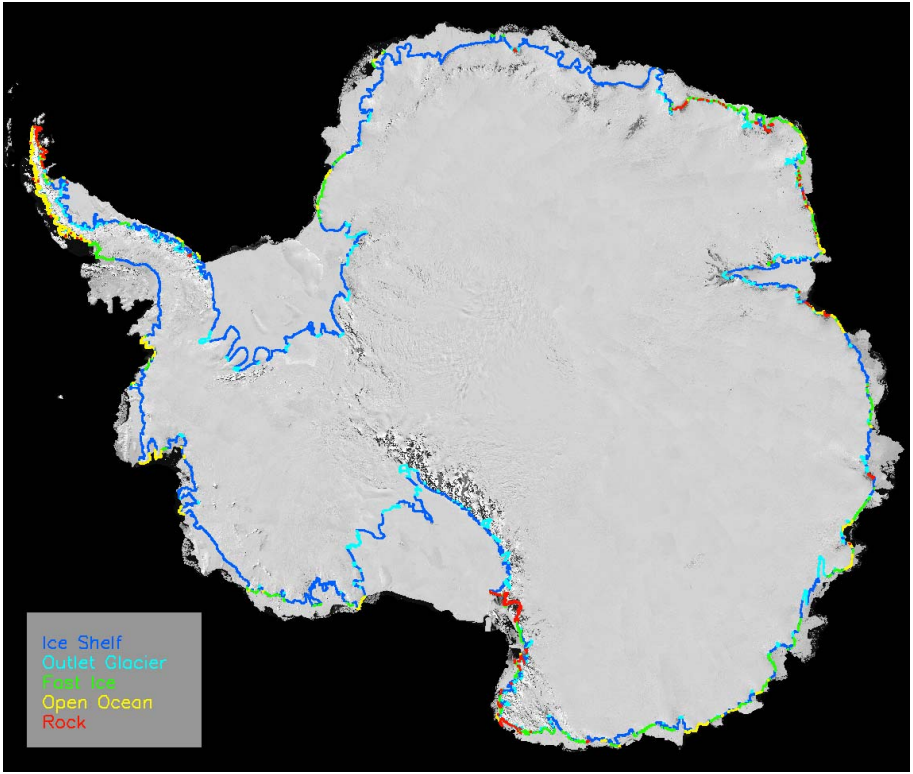

Fig. 5. The ASAID grounding line displayed on the Landsat Image Mosaic of Antarctica. Line color represents the transition of ice transiting the grounding line, along with the corresponding percent frequency of occurrence: dark blue, Ice Shelf (61%); cyan, Outlet Glacier (13%); green, Fast Ice (10%); orange, Open Ocean (9%); and red, Rock (7%).

TCD
5, 183–227, 2011

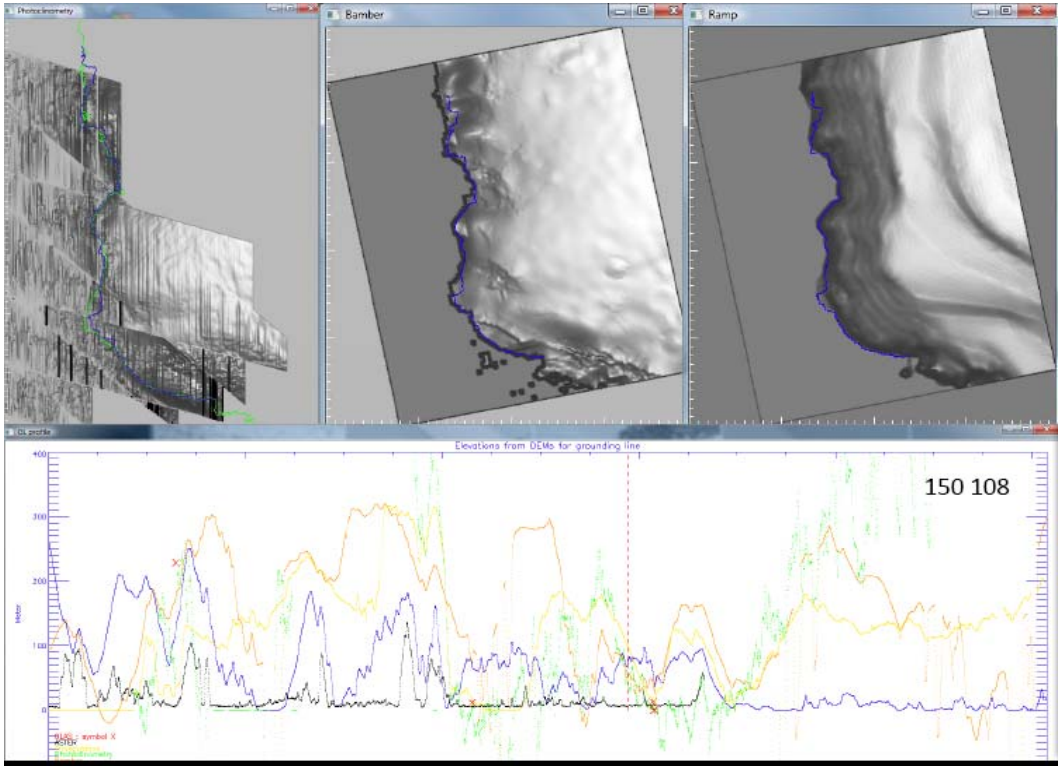

Fig. 6. Sample of screen display for elevation selection operation. Upper three windows are shaded relief versions of photoclinometric, altimetric and Radarsat DEM, rotated and illuminated to match the original Landsat sub-image. Blue line is the ASAID grounding line; green line is the MOA grounding line. Lower plots includes elevation profiles extracted from various DEMs with red X's being ICESat GLAS elevation values positioned where the ICESat profiles crossed the grounding line.

TCD
5, 183–227, 2011

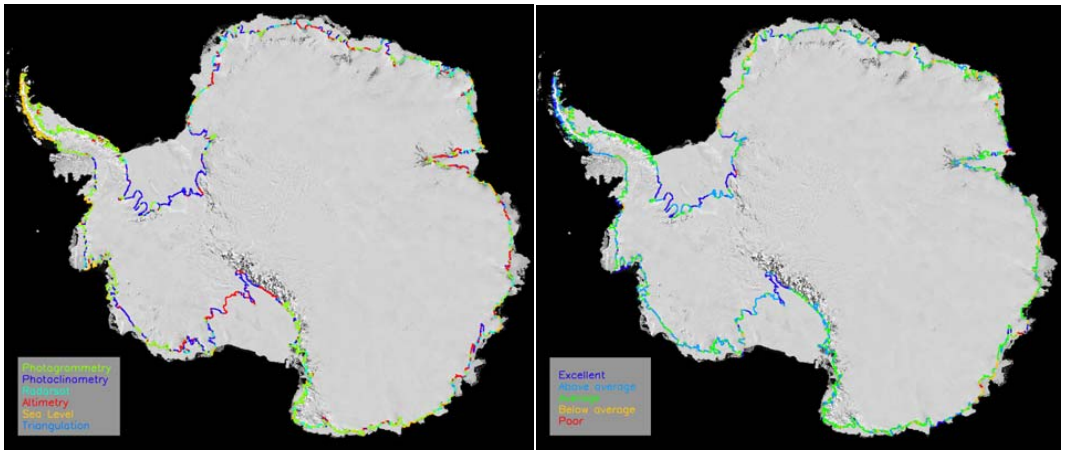

Fig. 7. The ASAID grounding line. (left) Colored lines represent the DEM source of selected elevation values, along with the corresponding percent frequency of occurrence: green, photogrammetry (33%); dark blue, photoclinometry (26%); cyan, Radarsat (17%); red, altimetry (13%); orange, sea level (9%); and light blue, triangulation (2%). (right) Colored lines represent the confidence in the selected elevations, along with the corresponding percent frequency of occurrence: dark blue, Excellent (18%); cyan, Above Average (36%); green, Average (40%); orange, Below Average (5%); and red, Poor (0.5%).

TCD
5, 183–227, 2011

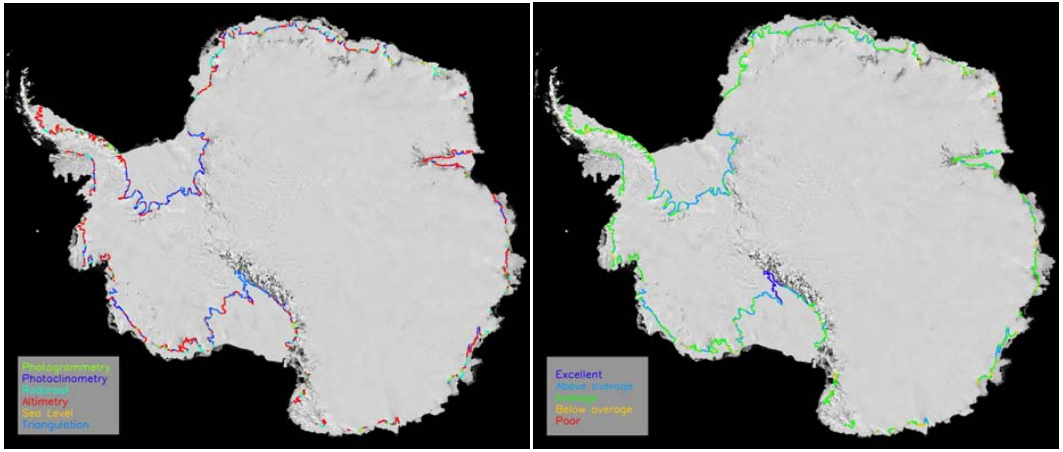

Fig. 8. The ASAID hydrostatic line. (left) Colored lines represent the DEM source of selected elevation values, along with the corresponding percent frequency of occurrence: green, photogrammetry (4%); dark blue, photoclinometry (37%); cyan, Radarsat (16%); red, altimetry (38%); orange, sea level (0.3%); and light blue, triangulation (5%). (right) Colored lines represent the confidence in the selected elevations, along with the corresponding percent frequency of occurrence: dark blue, Excellent (4%); cyan, Above Average (32%); green, Average (59%); orange, Below Average (4%); and red, Poor (0.1%).

TCD
5, 183–227, 2011

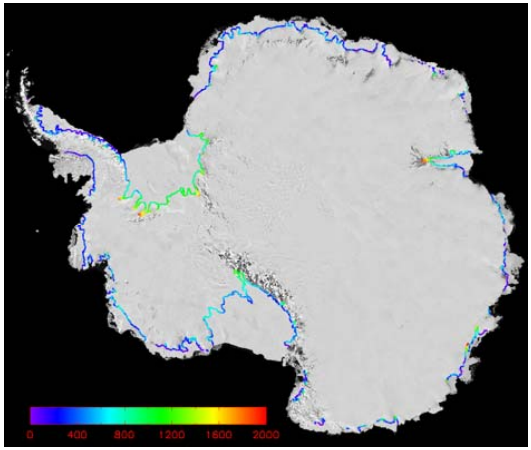

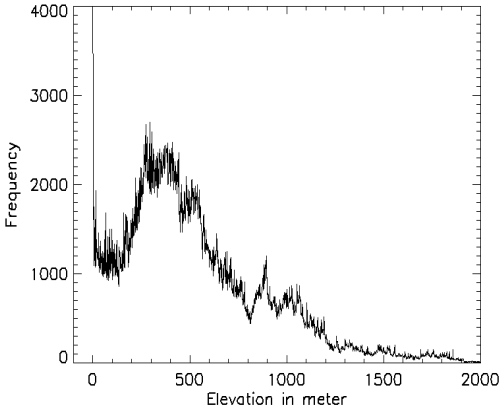

Fig. 9. Ice thickness calculated for the ASAID hydrostatic line and histogram of values. Conversion method is discussed in the text.

TCD
5, 183–227, 2011

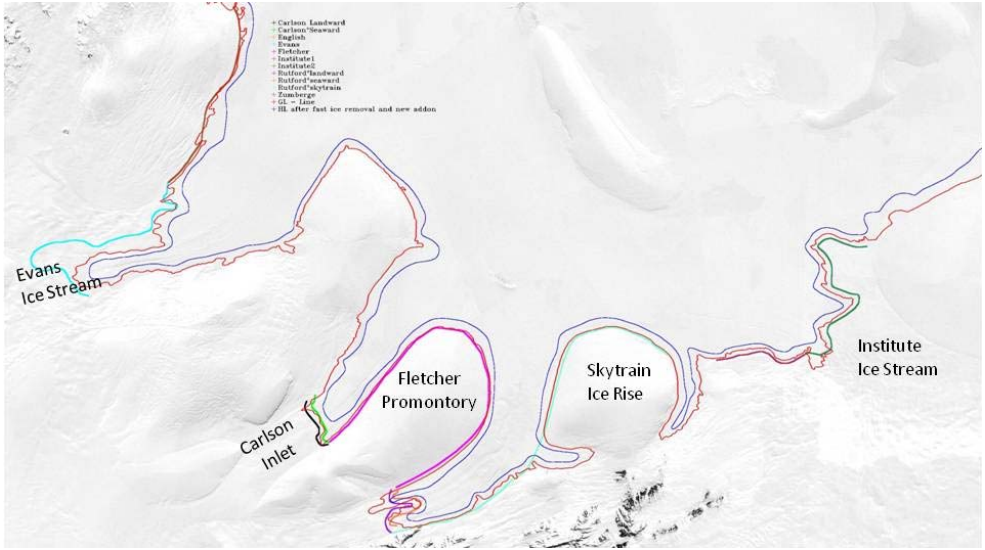

Fig. 10. Image map of region where validation study data were collected. Continuous red and blue lines are the ASAID grounding and hydrostatic lines, respectively. Shorter colored lines are flightlines following grounding deduced from interferometric SAR where field data of surface elevaton and ice thickness were collected.

TCD
5, 183–227, 2011

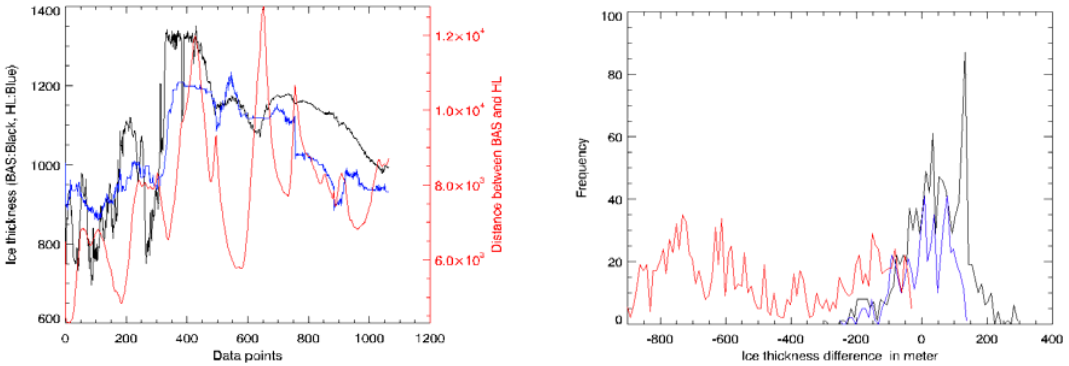

Fig. 11. (left) Profiles of ice thickness measured in the vicinity of Institute Ice Stream (cf. Fig. 10) by BAS airborne ice sounder (black) and derived from Eq. (3) along the ASAID hydrostatic line (blue). Red line (referenced to secondary axis) is distance separating BAS flightline from ASAID hydrostatic line. (right) Histograms of BAS ice thickness minus ASAID hydrostatic line ice thickness for three segments of the BAS validation flightline: north of Evans Ice Stream (blue); Fletcher Promontory (red); and Institute Ice Stream (black) (cf. Fig. 10).

TCD
5, 183–227, 2011

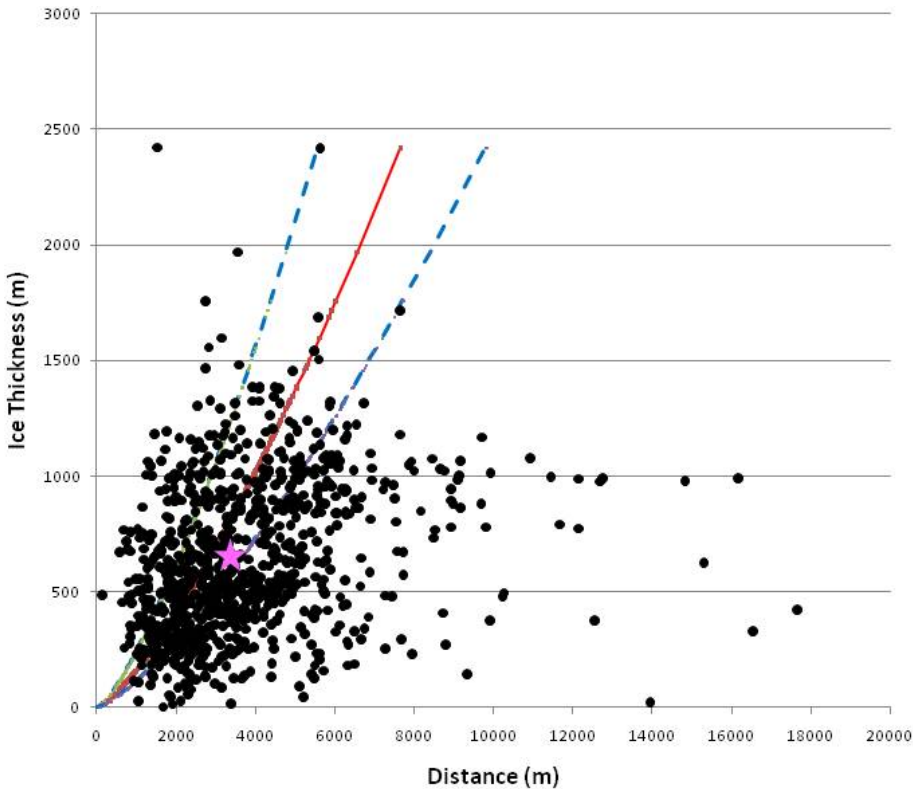

Fig. 12. Relationship of distance between ASAID grounding line and ASAID hydrostatic line to ice thickness derived as discussed in the text. Red line is theoretical relationship (Eq. 7) discussed in the text with blue dashed lines being one standard deviation from this theoretical relationship. Magenta star indicates the position occupied by the mean distance and mean ice thickness of all 930 points.

TCD
5, 183–227, 2011